Materials Today Energy 54 (2025) 102122

Contents lists available at ScienceDirect

Materials Today Energy

journal homepage: www.journals.elsevier.com/materials-today-energy/

DMSO-free solvent for high efficiency perovskite solar cells

Changzeng Ding [a,b,*], Yongqi Sun [a], Lianping Zhang [a], Qing Zhang [c], Ronald Österbacka [b], Chang-Qi Ma [a,**]

[a] i-Lab & Printable Electronics Research Center, Suzhou Institute of Nano-Tech and Nano-Bionics, Chinese Academy of Sciences, Ruoshui Road 398, SEID, SIP, Suzhou, PR China

[b] Physics and Center for Functional Materials, Faculty of Science and Technology, Åbo Akademi University, Henriksgatan 3, Turku, 20500, Finland

[c] Vacuum Interconnected Nanotech Workstation, Suzhou Institute of Nano-Tech and Nano-Bionics, Chinese Academy of Sciences, Ruoshui Road 398, SEID, SIP, Suzhou, PR China

ARTICLE INFO

Keywords:
DMSO free
Solvent engineering
PSCs
TFPS

ABSTRACT

Solvent engineering is critical for optimizing perovskite solar cell performance. While DMSO is widely used to control crystallization, its high boiling point often leaves residual solvent, leading to interfacial issues and reduced stability. In this work, we replace DMSO with trifluoropropyltrichlorosilane (TFPS) as a novel additive in DMF to address these challenges. TFPS incorporation introduces microstructural voids in PbI_2 films, enhancing ammonium halide infiltration and promoting the formation of larger perovskite grains. TOF-SIMS depth profiling shows that TFPS accumulates at the buried interface, improving film density, as supported by SEM results. Devices fabricated with TFPS-doped DMF exhibit improved performance, achieving a power conversion efficiency of 24.49 %, outperforming those made with pure DMF or DMF:DMSO. Impedance spectroscopy and Mott-Schottky analysis confirm that TFPS enhances interfacial charge properties, increasing built-in potential and reducing recombination. This study demonstrates a promising DMSO-free solvent strategy to improve perovskite film quality and device efficiency.

1. Introduction

Perovskite solar cells (PSCs) have gained significant attention due to their high efficiency [1], low cost [2], and simple fabrication processes [3,4]. In the past 15 years, PSCs have achieved power conversion efficiency (PCE) exceeding 27 % [5], making them strong competitors to traditional silicon solar cells. For the development of PSCs, the precursor plays a key role in forming the desired perovskite phase [6], directly affecting crystallization, and thus impacting the efficiency and stability of PSCs [7,8]. A major research challenge in PSCs is the scalable fabrication of large-area perovskite films with uniform morphology and high crystallinity [9–11]. Among the various factors influencing film quality, solvent selection is particularly critical, as it directly impacts nucleation, crystal growth, and overall film formation dynamics [12–15]. Conventional solvent systems often result in non-uniform crystallization or incomplete film coverage when applied to large substrates [12]. Therefore, solvent engineering has become a key strategy for achieving high-performance PSCs [15–17]. The choice of solvent not only determines the solubility of precursor salts but also governs the formation of intermediate phases and the kinetics of final crystallization. Currently, binary solvent systems such as DMF:DMSO or GBL:DMSO are commonly employed [18]. These combinations promote the formation of stable intermediate complexes (PbI_2·DMSO) in precursor solutions, which then convert into high-quality perovskite films during anti-solvent treatment or thermal annealing [19]. Such methods effectively regulate grain growth, resulting in uniform, dense, and pinhole-free films, which are crucial for device efficiency and stability. However, the high boiling point of DMSO (189 °C) presents several notable drawbacks [20–22]. Firstly, it is difficult to fully evaporate, often leaving residual solvent within the film, especially under low-temperature or insufficient annealing conditions. These residues can weaken interfacial adhesion and introduce barriers to charge transport, ultimately compromising device efficiency and stability [23]. Secondly, due to its slow evaporation rate and high viscosity, the film formation process becomes highly sensitive to environmental factors such as humidity and temperature, leading to poor reproducibility [24].

---

* Corresponding author. i-Lab & Printable Electronics Research Center, Suzhou Institute of Nano-Tech and Nano-Bionics, Chinese Academy of Sciences, Ruoshui Road 398, SEID, SIP, Suzhou, PR China.

** Corresponding author.

E-mail addresses: czding2017@sinano.ac.cn (C. Ding), cqma2011@sinano.ac.cn (C.-Q. Ma).

https://doi.org/10.1016/j.mtener.2025.102122
Received 3 September 2025; Received in revised form 28 October 2025; Accepted 3 November 2025

More critically, in scalable fabrication techniques such as slot-die coating or spray coating, the high boiling point of DMSO hinders rapid drying, thereby limiting its suitability for industrial-scale production [25].

Identifying effective substitutes for DMSO is essential for achieving scalable manufacturing and improved production efficiency. Researchers have explored various alternative solvent systems. For example, Noel et al. [26] utilized a low-boiling-point solvent mixture of acetonitrile and methylamine to fabricate high-quality and uniform perovskite films, achieving device efficiencies exceeding 18 % through optimized crystallization processes. Similarly, Zhang et al. [13] proposed using N,N′-dimethylpropyleneurea (DMPU) as a replacement for DMSO in Sn-Pb perovskite formulations combined with DMF. DMPU, featuring a lower boiling point and weaker coordination ability, reduces solvent residues and enhances film crystalline. Additionally, the chemical stability of DMPU helps suppress the oxidation of Sn (II) to Sn (IV), thereby enhancing film and device stability.

Recently, increasing attention has been directed toward developing environmentally friendly fabrication processes for perovskite solar cells. For instance, solvent-free or low-toxicity solvent strategies have been demonstrated to reduce environmental impact while maintaining high device performance [27]. In addition to optimizing the solvent system, introducing functional additives into the perovskite precursor solution offers another effective strategy to regulate film formation and improve device performance. Trichloro(3,3,3-trifluoropropyl)silane (TFPS) has been widely employed as an interfacial modifier and hydrophobic surface treatment in PSCs. By reacting with surface hydroxyl groups to form covalent bonds, TFPS can effectively passivate interfacial defects, regulate energy level alignment, and reduce non-radiative recombination [28]. These effects contribute to enhanced open-circuit voltage (V_{OC}) and fill factor (FF). Moreover, the trifluoro propyl chain imparts strong hydrophobicity to the surface, which can effectively suppress moisture permeation, thereby improving the stability of perovskite films under humid conditions. In this study, TFPS was incorporated into the perovskite precursor solution to explore its impact on film morphology and overall device performance. Here, we combine DMSO-free solvent engineering with functional additive incorporation to simultaneously optimize crystallization dynamics and interfacial properties. By integrating TFPS directly into a DMF-based solvent system, we obtain perovskite films with enhanced crystallinity and significantly reduced defect density. This strategy establishes a scalable route toward stable, high-performance perovskite solar cells beyond the limitations of conventional DMSO-based processing.

2. Results and discussion

TFPS was added to the perovskite precursor solution via one-step spin-coating, immediately causing flocculent precipitates due to its rapid reaction with the solvent (DMF or DMSO). Basenko et al. reported [29]that the reaction of $EtSi(H)Cl_2$ with DMSO proceeds through the formation of reactive silanone intermediates, EtSi(H)=O and EtSi(Cl)=O, generated via nucleophilic attack of DMSO oxygen on the silicon center followed by chloride elimination. Subsequent condensation of these silanones affords oligoethyl(hydro)cyclosiloxanes. Similar reaction of dichloro(methyl)(vinyl)silane reacts with DMSO in the presence of octamethyltrisiloxane to form cyclooligomethyl(vinyl)siloxanes (MeViSiO)n ($n = 3$–6) [30]. The reaction of chlorosilane with DMSO was further developed for the synthesis of ClRR'Si-O-SiRR' (R = Cl, H, CH_3; R' = CH_3, Et, $ClCH_2$, Vin, Ph) [31]. Following this study, we speculate that TFPS react with DMSO to produce siloxane oligomers, HCl, leading to white precipitate formation (Fig. S1a). With increasing TFPS concentration, the solution color gradually changed from yellow to brown (Fig. S1b), indicating ongoing chemical changes. Although the addition of TFPS had little influence on the morphology of perovskite films prepared by the one-step method (Fig. S2), these reactions may potentially interfere with film formation. Therefore, to avoid the reaction between TFPS and DMSO, a two-step method using pure DMF as the solvent was adopted for perovskite film fabrication. As illustrated in Fig. S3a, the reference solution (noted as Ref.) exhibited milky at room temperature, indicating incomplete dissolution of PbI_2 in DMF. Upon the addition of 3, 5, 10, 15, and 20 μL of TFPS to 1 mL of the PbI_2 solution, the mixture gradually became transparent, demonstrating that TFPS enhanced the solubility of PbI_2 in DMF. This is attributed to a reaction between TFPS and trace water in DMF, generating -OH groups and small amounts of HCl [32], which promote PbI_2 dissolution [33].

Perovskite films were then prepared using the two-step method (Fig. S3b). To evaluate the impact of TFPS-doped DMF on device performance, planar n-i-p structured perovskite solar cells were fabricated using SnO_2 and Spiro-OMeTAD as the electron and hole transport layers, respectively (Fig. 1a). For comparison, a DMF:DMSO (4:1 v/v) mixed solvent was also employed. Fig. 1b shows the *J-V* characteristics of the resulting devices. The cell fabricated with a DMF-based perovskite film exhibited a power conversion efficiency (PCE) of only 11.86 %, with a V_{OC} of 0.791 V, a J_{SC} of 25.07 mA/cm^2, and FF of 59.99 %. In contrast, the TFPS-doped DMF solvent (2 μL TFPS in 1 mL DMF) achieved a significantly improved PCE of 24.29 %, with a V_{OC} of 1.169 V, J_{SC} of 25.67 mA/cm^2, and FF of 84.49 %. The device based on the DMF:DMSO mixed solvent also showed enhanced performance, reaching a PCE of 22.77 %, with a V_{OC} of 1.122 V, J_{SC} of 25.26 mA/cm^2 and FF of 80.41 %. The slightly lower efficiency of the DMF:DMSO device can be attributed to the strong coordination between DMSO and Pb^{2+} ions, which slows solvent evaporation and leads to residual intermediate phases and incomplete crystallization, thereby limiting film quality and device performance. The detailed photovoltaic parameters of the devices are summarized in Table 1, and the statistical distribution of device performance with three different solvents are shown in Fig. 1c and d. The photovoltaic parameters show a clear improvement from DMF to DMF: DMSO and TFPS-doped DMF. The TFPS-doped DMF devices exhibit higher median values and narrower distributions, indicating enhanced device reproducibility.

To investigate the morphology of PbI_2 and perovskite films prepared with different solvents, we used SEM to characterize the surface morphologies. The results are shown in Fig. 2. Fig. 2a–c shows the surface morphologies of PbI_2 films prepared with DMF, TFPS doped DMF and DMF:DMSO solvents. As shown in Fig. 2a the PbI_2 film contains numerous voids and exhibits poor film compactness. In Fig. 2b, the introduction of TFPS improves the compactness of the PbI_2 films, however in the films display more larger voids. In Fig. 2c, the film prepared from the DMF:DMSO mixed solvent shows a highly compact morphology with minimal void formation. The effect of different concentrations of TFPS doped in DMF on the morphology of PbI_2 is shown in Fig. S4.

Previous studies have shown that the crystallinity of the PbI_2 layer significantly affects the quality of perovskite films in two-step fabrication. Porous PbI_2 films allow better infiltration of organic halides and more complete reactions, but can lead to uneven conversion and small, low-crystallinity grains. In contrast, compact PbI_2 films support the growth of larger, more crystalline grains, but may block halide penetration, causing incomplete conversion [34]. To investigate how PbI_2 film morphology influences perovskite crystallization, a mixed solution of FAI:MACl was applied onto PbI_2 films, followed by spin-coating and annealing at 150 °C for 10 min. SEM images (Fig. 2d–f) illustrate top surface morphologies of perovskite films fabricated with different solvents. The pure DMF-derived film (Fig. 2d) exhibited a smooth surface with distinct grain boundaries and no visible residual PbI_2, indicating effective precursor infiltration and complete reaction. With TFPS doping (Fig. 2e), the grain growth and uniform film structure occurred, though slight PbI_2 residues persisted. In contrast, the film derived from DMF: DMSO solvent (Fig. 2f) had poor infiltration due to dense PbI_2, causing substantial residual PbI_2 and incomplete perovskite conversion. The effect of different concentrations of TFPS doped in DMF on the morphology of perovskite film is shown in Fig. S5. The statistics of

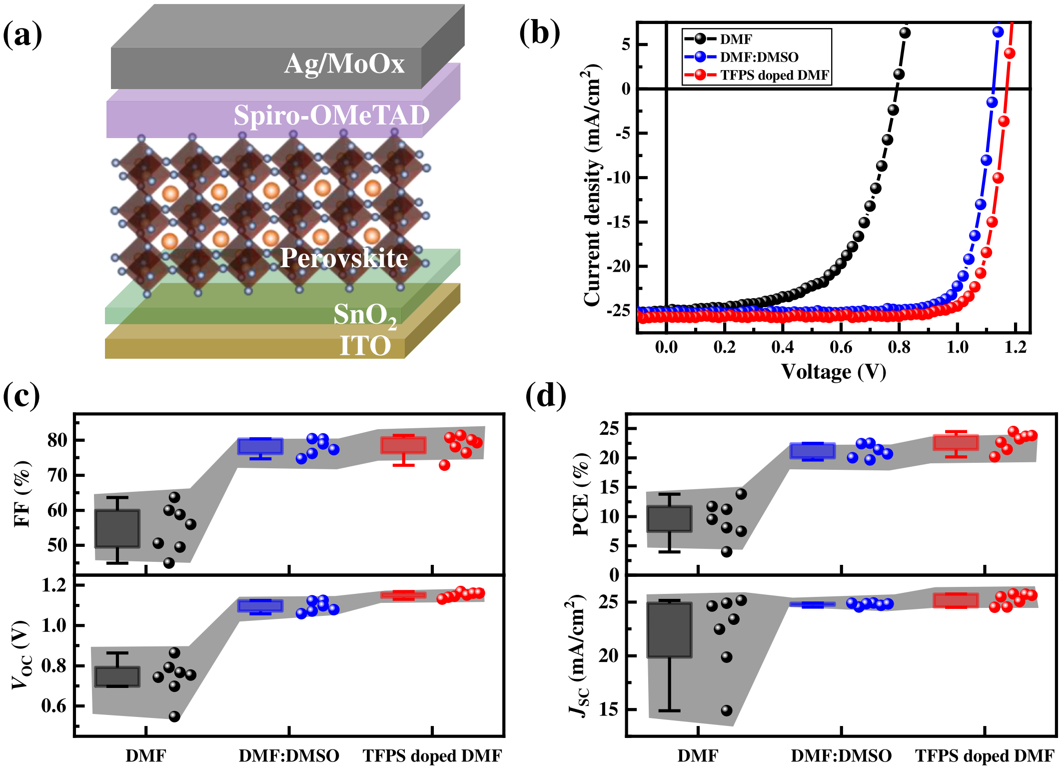

Fig. 1. (a) n-i-p type PSCs structure. (b) *J-V* curves of PSCs with different solvent systems. Distribution of device performance with different solvent systems (c) V_{OC} and FF (d) J_{SC} and PCE.

Table 1
The photovoltaic performance data of PSCs fabricated by different solvents.

	V_{OC} (V)	J_{SC} (mA/ cm^2)	FF (%)	PCE (%)
DMF	0.791 0.719 ± 0.105	25.07 22.17 ± 3.70	59.99 54.76 ± 6.66	11.86 9.38 ± 3.25
DMF:DMSO	1.122 1.092 ± 0.028	25.26 24.77 ± 0.14	80.41 77.96 ± 2.32	22.77 21.10 ± 1.20
TFPS doped DMF	1.169 1.150 ± 0.013	25.67 25.23 ± 0.54	81.39 78.38 ± 2.95	24.49 22.77 ± 1.50

efficiency with different TFPS doping are shown in Fig. S6, with the highest PCE achieved at 0.2 %-TFPS doping. These results indicate that the introduction of moderate voids in the TFPS-modified PbI$_2$ film enhances the infiltration of organic precursors, enabling complete perovskite conversion. These voids are subsequently filled during crystal growth, yielding a dense and high-quality perovskite film.

To understand how solvent engineering affects the buried interface of perovskite film. The buried interface morphology of the perovskite films is shown in Fig. 2 g-i. For the film prepared using DMF solvent (Fig. 2g), the bottom surface exhibits grain boundaries, numerous pinholes, and small grain sizes. This indicates that the perovskite crystallized too rapidly, preventing the formation of a compact buried interface. In contrast, the buried interface of the TFPS-doped film (Fig. 2h) appears denser, with no obvious grain boundaries and only a few small voids, which may be attributed to the presence of polymeric structures formed by TFPS at the interface. The buried interface formed from the DMF:DMSO mixed solvent (Fig. 2i) also shows relatively good compactness but contains more voids, resulting in more defects at the buried interface.

Although the surface SEM image of the TFPS-based film (Fig. 2e) shows slightly more visible surface features, the buried-interface SEM (Fig. 2h) reveals smoother and more compact contact with the substrate compared with the reference and control films (Fig. 2g and i). This indicates that TFPS effectively reduces buried-interface defects and improves interfacial passivation, which facilitates charge extraction and accounts for the superior device performance despite the relatively rougher surface morphology.

TOF-SIMS depth profiling of F$^-$ signal (Fig. S7) reveals a significant accumulation of TFPS at the bottom interface of the perovskite film processed with TFPS-doped DMF, The F$^-$ element primarily originates from the trifluoromethyl groups of TFPS. In contrast, films fabricated using pure DMF or DMF:DMSO mixed solvents show only weak signals. These results suggest that TFPS species are predominantly localized at the buried interface, which may account for the observed reduction in interfacial defects upon TFPS incorporation.

To further investigate the impact of different solvent engineering on the crystallization of PbI$_2$ and perovskite films, X-ray diffraction (XRD) was employed to characterize. Fig. 3a revealed that PbI$_2$ films from different solvents showed a similar preferred orientation along the (001) plane (2θ ~ 12.889°), indicating consistent crystal structure regardless of solvent. However, crystallite sizes calculated via Scherrer equation, $D = K\lambda/(\beta \cos\theta)$, where K is the shape factor (0.9), λ is the X-ray wavelength, β is the full width at half maximum (FWHM) of the diffraction peak, and θ is the Bragg angle [35]. The crystallite sizes varied significantly: 47.4 nm (DMF), 43.9 nm (TFPS-doped DMF), and 61.4 nm (DMF:DMSO), suggesting superior crystallinity with DMF: DMSO. For perovskite films, diffraction peaks shifted slightly, indicating lattice contraction and varying crystallinity, as shown in Fig. 3b. The TFPS-doped perovskite film produced the largest crystallite size (85.3 nm) with improved compactness and grain size, whereas the perovskite obtained from DMF:DMSO yielded the smallest crystallites (~21 nm).

To gain deeper insight into the effects of different solvents on the crystallization behavior of both the PbI$_2$ and perovskite films, two-dimensional grazing-incidence wide-angle X-ray scattering (GIWAXS)

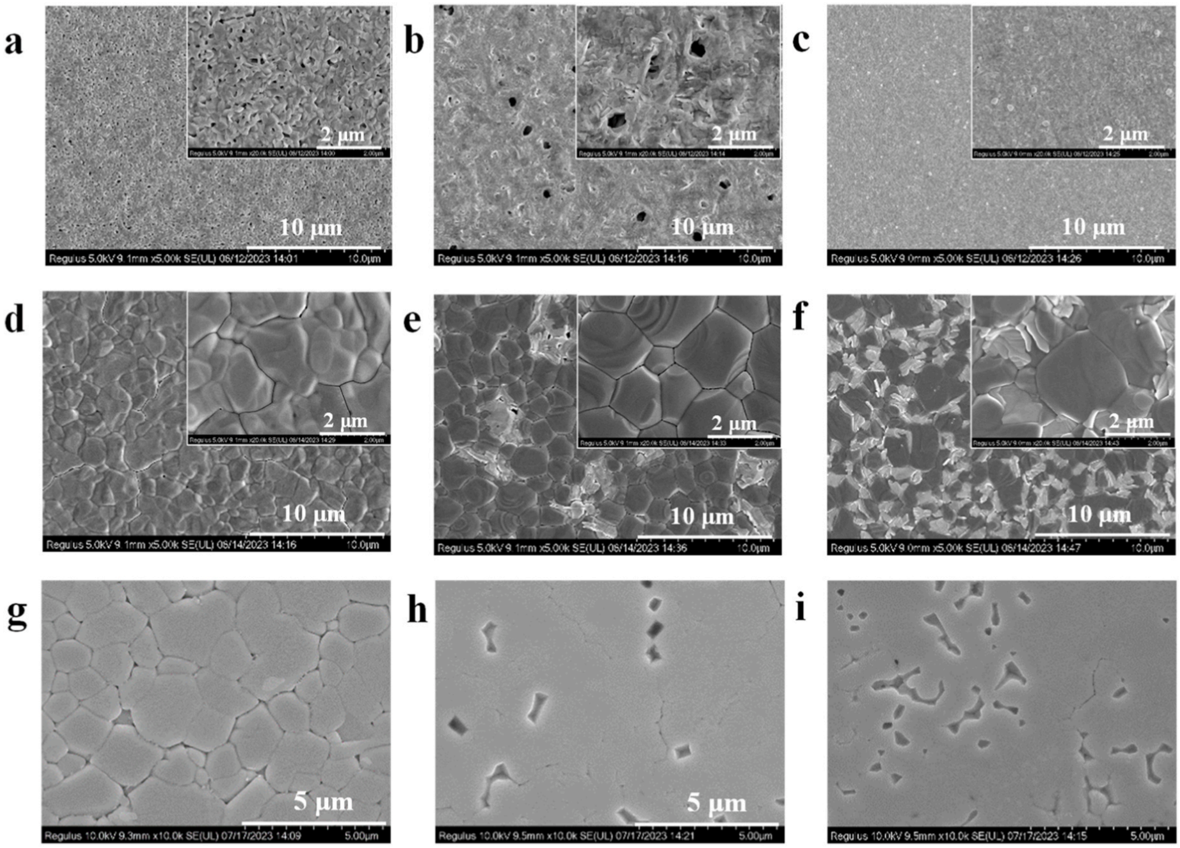

Fig. 2. SEM images of PbI_2 films (top row) and their corresponding perovskite films, top surface morphology (middle row) and buried surface morphology (bottom row), prepared using (a, d, g) DMF, (b, e, h) TFPS-doped DMF, and (c, f, i) DMF: DMSO.

was employed. The GIWAXS patterns of PbI_2 films (Fig. 3c–e) and perovskite films (Fig. 3f–h) prepared using DMF, TFPS-doped DMF, and DMF:DMSO mixed solvent, respectively. In the PbI_2 films, distinct diffraction features are observed in all PbI_2 films prepared from different solvent systems. Among them, the film derived from TFPS-doped DMF (Fig. 3d) shows localized diffraction arcs, indicating a well-defined preferred orientation of PbI_2 layers compared with those from pure DMF (Fig. 3c) and DMF:DMSO (Fig. 3e). The film prepared from DMF: DMSO exhibits weaker and more diffuse ring-like diffraction, indicating a largely randomly oriented polycrystalline structure. The strong coordination ability of DMSO with Pb^{2+} forms stable $PbI_2{\cdot}(DMSO)_x$ complexes, which slow down the crystallization process during solvent evaporation. As shown in Fig. S8, the PbI_2 film exhibits stronger diffraction in the out-of-plane direction, suggesting that the residual PbI_2 is preferentially oriented perpendicular to the substrate. The GIWAXS patterns of the perovskite films further highlight the influence of the precursor solvent on final perovskite film quality. Notably, the perovskite film derived from the DMF:DMSO solvent (Fig. 3h) displays continuous and uniform diffraction rings, indicating high crystallinity, which reflect uniform nucleation and oriented crystal growth. While the perovskite film obtained from TFPS-doped DMF solvent (Fig. 3g) shows enhanced crystallinity in the PbI_2 stage, its effect on perovskite crystallization is less pronounced than that of the DMF:DMSO solvent. This suggests that the composition of the precursor solvent plays a key role in determining the crystallization kinetics of the perovskite film.

To further evaluate the effect of TFPS on film stability, perovskite films were stored in ambient air with a relative humidity of approximately 60 % (Fig. S9). The film prepared from pure DMF gradually changed from dark black to yellow within 240 min, indicating moisture-induced degradation and a phase transition to the non-perovskite δ-phase. In contrast, the perovskite films prepared from TFPS-doped DMF and DMF:DMSO retained their dark color and smooth surface, demonstrating much better resistance to humidity. These results indicate that both TFPS-doped and DMF:DMSO-based perovskite films exhibit good humidity stability under ambient conditions.

To investigate the interfacial charge transport behavior in PSCs prepared with different solvent systems, impedance spectroscopy (IS) and Mott-Schottky analysis were employed to elucidate the interfacial charge transport and recombination behavior of the devices fabricated with different solvent systems. The Nyquist plots, as shown in Fig. 4a, and the corresponding fitted parameters (as shown in Table S1) provide insightful information about the series resistance (Rs), charge transfer resistance (Rtr), and recombination resistance (Rrec) at the interfaces.

As shown in Table S1, the device prepared with the DMF:DMSO mixed solvent exhibits the lowest Rs (28.9 Ω), indicating enhanced ionic conductivity and more efficient ion migration in the perovskite layer. Meanwhile, this system also demonstrates the lowest Rtr (6.09 Ω), which suggests significantly improved electronic charge transport at the perovskite/electrode interface. In contrast, TFPS doped DMF leads to a markedly increased Rtr (82.83 Ω), implying hindered charge transfer by the existence of silane polymer at the buried interface, which confirmed by SEM and TOF-SIMS results. In terms of recombination dynamics, the DMF:DMSO and TFPS doped DMF systems both show significantly elevated Rrec values (1298 Ω and 1031 Ω, respectively) compared to the pristine DMF solvent (146 Ω). This indicates that both the DMSO coordination and the presence of TFPS dopants effectively suppress charge recombination processes and correlates with their higher V_{OC} values [36,37]. Correspondingly, the lower values of Crec observed in these systems further support a reduced density of interfacial trap states or slower recombination kinetics.

Fig. 4b presents the Mott-Schottky plots of the devices, which were used to examine differences in carrier concentration and built-in electric

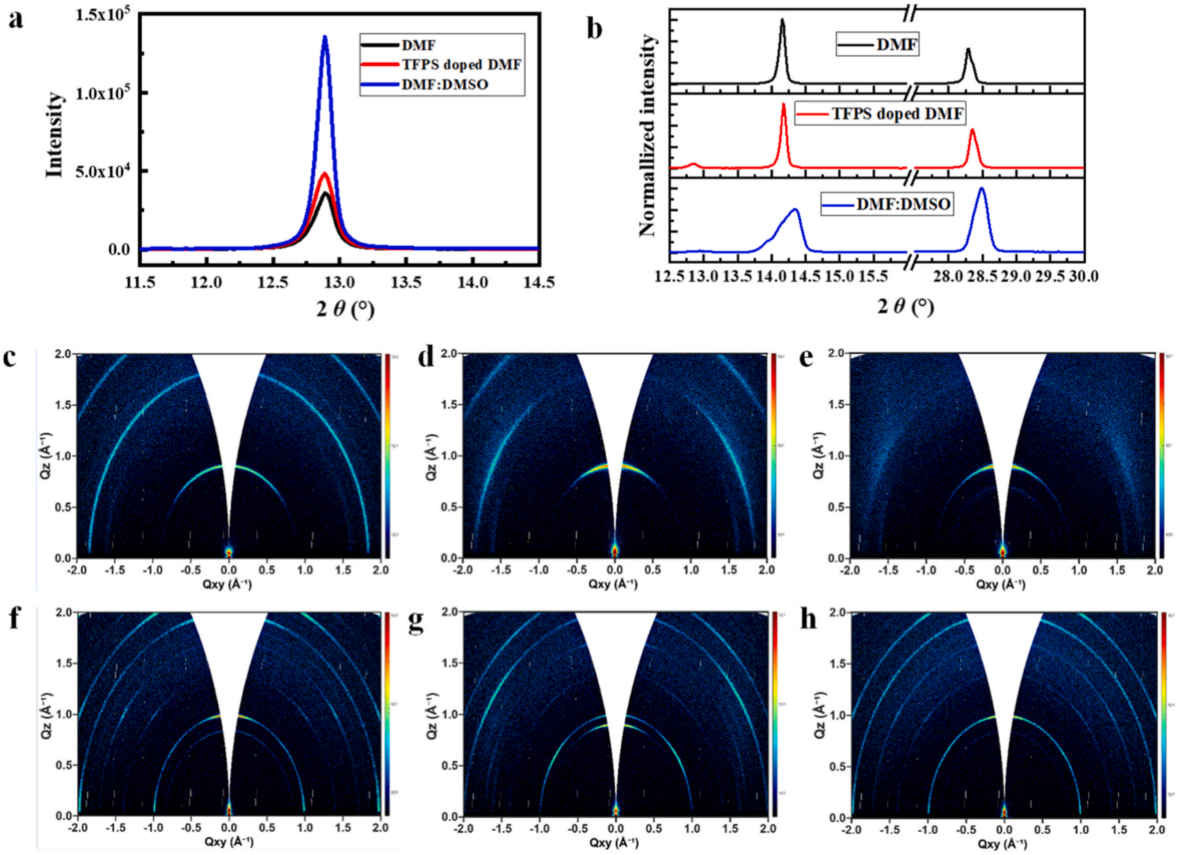

Fig. 3. X-ray diffraction (XRD) patterns of (a) PbI_2 films and (b) perovskite films prepared using different solvent systems. GIWAXS patterns of (c–e) PbI_2 films and (f–h) corresponding perovskite films prepared under different solvent conditions. PbI_2 was dissolved in: (c, f) DMF, (d, g) TFPS-doped DMF, and (e, h) DMF:DMSO.

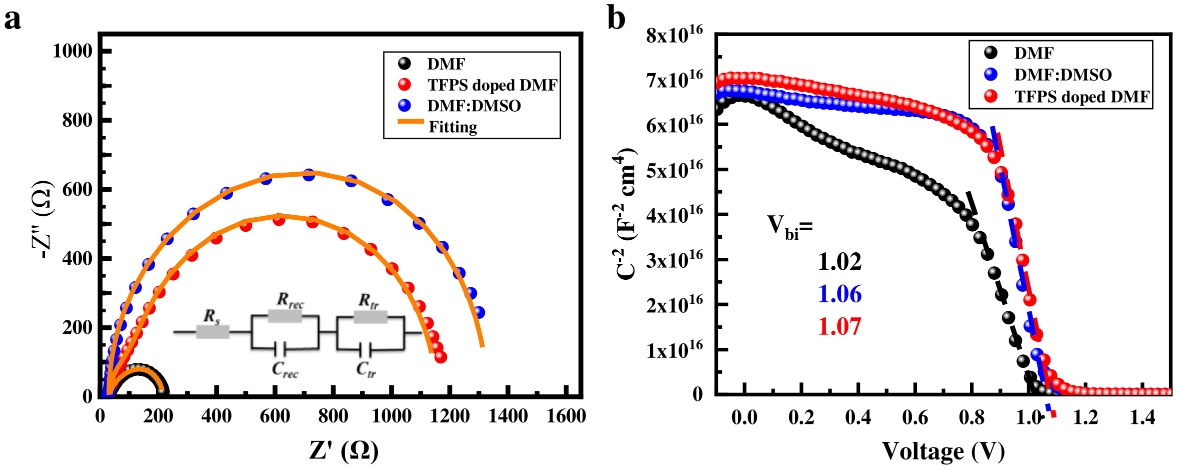

Fig. 4. (a) Impedance spectra of perovskite solar cells prepared with different solvent systems, measured in the dark under an applied bias equal to the V_{OC}. (b) Mott-Schottky plots of the corresponding devices, measured under dark conditions.

field (V_{bi}). The intersection points of the linear fit with the voltage axis indicate the magnitude of V_{bi}. The TFPS-doped device exhibited the highest built-in potential of 1.07 V, followed by the DMF:DMSO (1.06 V) and DMF-based (1.02 V) devices, consistent with the V_{OC} trends.

In addition, the trap-state density (N) was estimated using the following relation [38]:

$$N=\frac{-2\left(dC^{-2}/dV\right)^{-1}}{q\varepsilon\varepsilon_0}$$

where q is the elementary charge, A is the effective area of the device, C is the capacitance, and V is the applied voltage. Fitting the linear region of the Mott-Schottky plot provides insight into the overall carrier density and trap-state distribution, further elucidating the impact of solvent engineering on device performance. The calculated trap-state densities for the TFPS-doped DMF and DMF:DMSO systems were 3.00×10^{16} cm^{-3} and 3.26×10^{16} cm^{-3}, respectively, both significantly lower than that of the DMF based device (1.86×10^{17} cm^{-3}). This reduction indicates a suppression of deep-level trap states. The EIS and Mott-Schottky analyses demonstrate that both TFPS doping and the use of a

DMF:DMSO mixed solvent can markedly improve the interfacial impedance characteristics and energy-level alignment in perovskite solar cells. These improvements ultimately lead to higher device efficiency.

3. Conclusion

In this work, the influence of TFPS doping on the morphology and crystallinity of PbI_2 and perovskite films was systematically investigated. The results demonstrate that an appropriate amount of TFPS doping can introduce microstructural voids within the PbI_2 film, which facilitates the infiltration of FAI:MACl solutions and provides sufficient space for perovskite crystal growth. As a result, TFPS-doped perovskite films exhibit larger grain sizes. TOF-SIMS analysis revealed that TFPS is primarily localized at the buried interface of the perovskite film. SEM images further confirmed that TFPS doping reduces the density of interfacial voids, leading to a denser and more uniform buried interface. Compared to conventional PSCs fabricated with DMF:DMSO mixed solvents, the TFPS-doped devices achieved a significantly higher PCE of 24.49 %, whereas the DMF-based device showed a much lower PCE of 11.86 %. Impedance spectroscopy and Mott-Schottky analysis indicated that TFPS doping increases interfacial recombination resistance and suppresses non-radiative recombination at the interface. Furthermore, it enhances the built-in electric field of the device, contributing to improved V_{OC} and FF. This work proposes a novel solvent engineering strategy for perovskite fabrication, where TFPS doping in DMF effectively replaces the conventional high-boiling-point solvent DMSO. The findings provide new insights and a promising direction for the development of future perovskite precursor solvent systems.

4. Experimental section

4.1. Materials

The SnO_2 colloid solution was purchased from Alfa Aesar (tin (IV) oxide, 15 wt% in H_2O colloidal dispersion). PbI_2, $PbBr_2$, CsI, Formamidinium iodide (FAI), methylammonium bromide (MABr), n-Octylammonium Iodide (OAI), Lithium bis(trifluoromethanesulphony)imide (LiTFSI), Pyridine,4-(1,1-dimethylethyl)- (t-BP) and Spiro-OMeTAD were purchased from Xi'an Polymer Light Technology Corp′, Trichloro (3,3,3-trifluoropropyl)silane was purchased from TCI, dimethylformamide (DMF, purity>99 %), dimethyl sulfoxide (DMSO, purity>99 %), chlorobenzene (CB, purity>99 %) and isopropanol (IPA, purity>99 %) were purchased from J&K scientific. All materials were used directly.

4.2. Instruments and characterization

The current density-voltage (*J-V*) characters of solar cells were measured with a Keithley 2400 source meter in an N_2 glove box under a simulated sun AM 1.5 G (Newport VeraSol- 2 LED Class AAA Solar Simulator). SEM images were gained by a field-emission scanning electron microscope (S-4800) under an accelerating voltage of 5 kV–10 kV. The time-of-flight secondary ion mass spectrometry (TOF-SIMS 5–100) was measured with the pulsed primary ions from a Cs^+ (2 keV) liquid-metal ion gun for sputtering and a Bi^+ pulsed primary ion beam for analysis (30 keV). Electrical impedance spectroscopy (EIS) and Mott-Schottky (M − S) measurements were carried out on the electrochemical workstation (PGSTA302N). The EIS measure conditions were under dark and applied bias at open voltage; the frequency range is 0.1 Hz–10 MHz. The M − S plot measurement conditions were determined to be a 10 kHz frequency. The GIWAXS measurements were performed at a Xeuss 3.0 system. The photon energy was 9.24 keV (wavelength = 1.3414 Å), and the incident angles are 0.05° and 1°. The diffracted X-rays were collected by an Eiger 2R 1 M detector at 2000 mm. The XRD spectra (θ-2θ scans) were taken on a D8 powder X-ray diffraction system (D8 Advance) with Cu Kα ($\lambda = 1.5418$ Å) as the X-ray source. The scan range was 5–65° (2θ) with a step size of 0.02° and a scan rate of 2° min^{-1}.

4.3. Preparation of the solutions

The SnO_2 colloid solution (15 wt%) was diluted using deionized water to the concentration of 3 wt%. Then, the solution was stirred at room temperature for 2 h.

One step perovskite solution (CsFAMA):

The $Cs_{0.05}(FA_{0.85}MA_{0.15})_{0.95}Pb(I_{0.85}Br_{0.15})_3$ (CsFAMA) precursor solution was prepared by dissolving PbI_2 (548.6 mg), $PbBr_2$ (77.07 mg), FAI (190.12 mg), and MABr (21.84 mg) in a mixture solvent of DMF/DMSO (1 mL. 4:1 v/v). Then, 34 μL CsI (2 M in DMSO) was added to a mixed perovskite solution, stirring for 2 h at room temperature. For TFPS doping solutions, add 1, 3, 5, 10 and 15 μL TFPS into 1 mL CsFAMA percussor solution.

Two step perovskite solution:

DMF based solution: 1.5 mmol PbI_2 was dissolved in 1 mL DMF solution and stirred at 70 °C for 5 h.

TFPS doped solution: add 0.5, 1, 2, 3, 5, 10, 15 and 20 μL TFPS into 1 mL DMF solution, and stirred at room temperature for 2 h. Then 1.5 mmol of PbI_2 was dissolved in the above-mentioned TFPS-doped DMF solvent, respectively, and stirred at 70 °C for 5 h.

DMF:DMSO based solution: 1.5 mmol PbI_2 was dissolved in 1 mL DMF:DMSO (volume ratio is 4:1) solution and stirred at 70 °C for 5 h.

FAI:MACl solution: 90 mg FAI and 15 mg MACl dissolved in 1 mL Isopropyl alcohol (IPA) and stirred at room temperature for 2 h.

The OAI solution was prepared by dissolving 5 mg OAI into 1 mL IPA, stirring for 2 h at room temperature. The Spiro-OMeTAD solution was prepared by dissolving 72.3 mg Spiro-OMeTAD into 1 mL chlorobenzene followed by the addition of 17.5 μL Li-TFSI (520 mg/mL in acetonitrile) and 29 μL t-BP, this solution was stirred overnight at room temperature.

4.4. Solar cell fabrication

ITO glass was cleaned by ultrasonic cleaning through detergent, and pure water was dried by N_2 gas flow, and cleaned by UV Ozone for 30 min. Then the substrate was spin-coated with a thin layer of SnO_2 nanoparticle from the SnO_2 colloid solution at 3000 rpm for 30 s, and annealed in ambient air at 150 °C for 30 min then the SnO_2 film was further treated by UV Ozone for another 10 min.

For the CsFAMA and TFPS doped perovskite films were prepared by one-step antisolvent method. The spin rate is 5000 rpm for 30 s with an accelerated speed of 1000 rpm. Before the end of 10 s, 200 μL of ethyl acetate was drop-coated to treat the perovskite films, and then the perovskite films were annealed at 120 °C for 30 min in a glovebox.

Two step perovskite film: 1.5 M PbI_2 in DMF, TFPS doped DMF and DMF:DMSO solvents were spin-coated onto SnO_2 at 1500 rpm for 30s, and annealed at 70 °C for 1 min, then cooled to room temperature. Then, FAI:MACl solution was spin-coated onto PbI_2 at spin rate of 1800 rpm. For 30 s, and the perovskite precursor film was annealing at 150 °C for 15 min in glovebox.

After the perovskite films cooling down to room temperature, the OAI solution was coated on perovskite films at 5000 rpm for 30s. Then, the spiro-OMeTAD solution was coated on perovskite films at 3000 rpm for 30 s with an accelerated speed of 3000 rpm. After that, the Spiro-OMeTAD layer was fully oxidized in the air with a humidity of 30 % for 5 h.

After the oxidation process, a fully covered MoO_3 was deposited on spiro-OMeTAD by thermal evaporation with a rate of 0.2 nm/s, with a thickness of 10 nm. Then, a structured Ag electrode was deposited on the MoO_3 layer with a rate of 0.5 nm/s, and a thickness of 150 nm. For the Al based cells, a thickness of 150 nm Al was deposited on MoO_3 with a rate of 2 nm/s.

CRediT authorship contribution statement

Changzeng Ding: Writing – review & editing, Writing – original draft, Visualization, Validation, Software, Resources, Project administration, Methodology, Investigation, Funding acquisition, Formal analysis, Data curation, Conceptualization. **Yongqi Sun:** Formal analysis, Data curation. **Lianping Zhang:** Methodology, Data curation. **Qing Zhang:** Methodology, Data curation. **Ronald Österbacka:** Writing – review & editing, Project administration, Methodology, Formal analysis. **Chang-Qi Ma:** Writing – review & editing, Supervision, Resources, Project administration, Funding acquisition.

Declaration of competing interest

The authors declare the following financial interests/personal relationships which may be considered as potential competing interests: Chang-Qi Ma reports financial support was provided by Jiangsu Science and Technology Program. Changzeng Ding reports financial support was provided by National Natural Science Foundation of China. Chang-Qi Ma reports financial support was provided by Science and Technology Program of Suzhou. If there are other authors, they declare that they have no known competing financial interests or personal relationships that could have appeared to influence the work reported in this paper.

Acknowledgements

The authors would like to acknowledge the financial support from National Natural Science Foundation of China (No.22409208), the Ministry of Science and Technology of the People's Republic of China (No. 2023YFB4204504), Jiangsu Science and Technology Program (BE2022023), Science and Technology Program of Suzhou (SWY2022004). C.Z acknowledges funding from the Magnus Ehrnrooth Foundation. We would also like to thank the technical support for Nano-X from Suzhou Institute of Nano-Tech and Nano-Bionics, Chinese Academy of Science.

Appendix A. Supplementary data

Supplementary data to this article can be found online at https://doi.org/10.1016/j.mtener.2025.102122.

Data availability

Data will be made available on request.

References

[1] Z. Xie, Y. Duan, M. Cheng, Y. Li, Z. Liu, H. Li, Y. Chen, Z. Zang, S. Liu, Q. Peng, High-efficiency perovskite solar cells enabled by guanylation reaction for removing MACl residual and In-Situ forming 2D perovskite, Angew. Chem. Int. Ed. 64 (7) (2025) e202419070, https://doi.org/10.1002/anie.202419070.

[2] P. Čulík, K. Brooks, C. Momblona, M. Adams, S. Kinge, F. Maréchal, P.J. Dyson, M. K. Nazeeruddin, Design and cost analysis of 100 MW perovskite solar panel manufacturing process in different locations, ACS Energy Lett. 7 (9) (2022) 3039–3044, https://doi.org/10.1021/acsenergylett.2c01728.

[3] B. Parida, A. Singh, A.K.K. Soopy, S. Sangaraju, M. Sundaray, S. Mishra, S.F. Liu, A. Najar, Recent developments in upscalable printing techniques for perovskite solar cells, Adv. Sci. 9 (14) (2022) 2200308, https://doi.org/10.1002/advs.202200308.

[4] J. Han, K. Park, S. Tan, Y. Vaynzof, J. Xue, E.W.-G. Diau, M.G. Bawendi, J.-W. Lee, I. Jeon, Perovskite solar cells, Nat. Rev. Methods Primers 5 (1) (2025) 3, https://doi.org/10.1038/s43586-024-00373-9.

[5] Best research-cell efficiencies. https://www.nrel.gov/docs/libraries/pv/best-research-cell-efficiencies.pdf, 2025.

[6] Z. Zhang, Y. Yang, Z. Huang, Q. Xu, S. Zhu, M. Li, P. Zhao, H. Cui, S. Li, X. Jin, X. Wu, M. Han, Y. Zhang, N. Zhao, C. Zou, Q. Liang, L. Xian, J. Hu, C. Zhu, Y. Chen, Y. Bai, Y. Li, Q. Chen, H. Zhou, B. Zhang, Y. Jiang, Coordination engineering with crown ethers for perovskite precursor stabilization and defect passivation, Energy Environ. Sci. 17 (19) (2024) 7182–7192, https://doi.org/10.1039/d4ee02124j.

[7] A. Rizzo, A. Listorti, S. Colella, Chemical insights into perovskite ink stability, Chem 8 (1) (2022) 31–45, https://doi.org/10.1016/j.chempr.2021.11.004.

[8] M. Li, C. Chen, The aging chemistry of perovskite precursor solutions, J. Phys. Chem. Lett. 16 (3) (2025) 754–765, https://doi.org/10.1021/acs.jpclett.4c03203.

[9] L. Chao, T. Niu, W. Gao, C. Ran, L. Song, Y. Chen, W. Huang, Solvent engineering of the precursor solution toward large-area production of perovskite solar cells, Adv. Mater. 33 (14) (2021) 2005410, https://doi.org/10.1002/adma.202005410.

[10] L. Tan, J. Zhou, X. Zhao, S. Wang, M. Li, C. Jiang, H. Li, Y. Zhang, Y. Ye, W. Tress, L. Ding, M. Grätzel, C. Yi, Combined vacuum evaporation and solution process for high-efficiency large-area perovskite solar cells with exceptional reproducibility, Adv. Mater. 35 (13) (2023) 2205027, https://doi.org/10.1002/adma.202205027.

[11] R. Yin, Y. Wu, Z. Huang, A.S. Vasenko, S. Xu, H. Zhou, Fabricating perovskite films for solar modules from small to large Scale, Adv. Funct. Mater. 35 (24) (2025) 2419184, https://doi.org/10.1002/adfm.202419184.

[12] Z. Jiang, B. Wang, W. Zhang, Z. Yang, M. Li, F. Ren, T. Imran, Z. Sun, S. Zhang, Y. Zhang, Z. Zhao, Z. Liu, W. Chen, Solvent engineering towards scalable fabrication of high-quality perovskite films for efficient solar modules, J. Energy Chem. 80 (2023) 689–710, https://doi.org/10.1016/j.jechem.2023.02.017.

[13] Z. Zhang, J. Liang, J. Wang, Y. Zheng, X. Wu, C. Tian, A. Sun, Y. Huang, Z. Zhou, Y. Yang, Y. Liu, C. Tang, C.C. Chen, DMSO-Free solvent strategy for stable and efficient methylammonium-free Sn–Pb alloyed perovskite solar cells, Adv. Energy Mater. 13 (17) (2023) 2300181, https://doi.org/10.1002/aenm.202300181.

[14] H. Kim, J.H. Seo, S. Palei, K. Seo, Solvent-additive coordination effect on lead-iodide precursor for enlarging grain size of perovskite film, ACS Appl. Energy Mater. 5 (1) (2022) 27–34, https://doi.org/10.1021/acsaem.1c03249.

[15] X. Zheng, Wenchi Kong, J. Wen, J. Hong, H. Luo, R. Xia, Z. Huang, X. Luo, Z. Liu, H. Li, H. Sun, Y. Wang, C. Liu, P. Wu, H. Gao, M. Li, A. Bui, Y. Mo, X. Zhang, G. Yang, Y. Chen, Z. Feng, H.T. Nguyen, R. Lin, L. Li, J. Gao, HairenTan, solvent engineering for scalable fabrication of perovskite/silicon tandem solar cells in air, Nat. Commun. 15 (1) (2024) 4907, https://doi.org/10.1038/s41467-024-49351-5.

[16] B.M. Gallant, P. Holzhey, J.A. Smith, S. Choudhary, K.A. Elmestekawy, P. Caprioglio, Igal Levine, A.A. Sheader, E.Y.-H. Hung, F. Yang, D.T.W. Toolan, R. C. Kilbride, K.-A. Zaininger, J.M. Ball, M.G. Christoforo, NakitaK. Noel, L.M. Herz, D.J. Kubicki, H.J. S, A green solvent enables precursor phase engineering of stable formamidinium lead triiodide perovskite solar cells, Nat. Commun. 15 (1) (2024) 10110, https://doi.org/10.1038/s41467-024-54113-4.

[17] E. Han, M. Lyu, E. Choi, Y. Zhao, Y. Zhang, J. Lee, S.-M. Lee, Y. Jiao, S.H.A. Ahmad, J. Seidel, J.S. Yun, J.-H. Yun, L. Wang, High-performance indoor perovskite solar cells by self-suppression of intrinsic defects via a facile solvent-engineering strategy, Small 20 (4) (2024) 2305192, https://doi.org/10.1002/smll.202305192.

[18] F. Meng, L. Cheng, F. Wang, K. Chen, Z. Sun, G. Wang, Sustainable green solvents for lead halide perovskites, Adv. Sustainable Syst. 9 (2) (2024) 2400695, https://doi.org/10.1002/adsu.202400695.

[19] I. Hwang, Challenges in controlling the crystallization pathways and kinetics for highly reproducible solution-processing of metal halide perovskites, J. Phys. Chem. C 127 (50) (2023) 24011–24026, https://doi.org/10.1021/acs.jpcc.3c05787.

[20] J.C. Hamill, J.C. Sorli, I. Pelczer, J. Schwartz, Y.-L. Loo, Acid-catalyzed reactions activate DMSO as a reagent in Perovskite precursor inks, Chem. Mater. 31 (6) (2019) 2114–2120, https://doi.org/10.1021/acs.chemmater.9b00019.

[21] Y. Ma, H. Cai, Y. Liu, B. He, H. Zhang, Y. Cheng, G. Liu, J. Zhao, Y.-B. Cheng, J. Zhong, Alleviation of precursor degradation induced by DMF/DMSO mixture for enhanced performance of perovskite solar cells, Angew. Chem. Int. Ed. (2025) e202504253, https://doi.org/10.1002/anie.202504253.

[22] J. Pascual, D.D. Girolamo, M.A. Flatken, M.H. Aldamasy, G. Li, M. Li, A. Abate, Lights and shadows of DMSO as solvent for tin halide perovskites, Chem. Eur J. 28 (12) (2022) e202103919, https://doi.org/10.1002/chem.202103919.

[23] S. Chen, X. Dai, S. Xu, H. Jiao, L. Zhao, J. Huang, Stabilizing perovskite-substrate interfaces for high-performance perovskite modules, Science 373 (2021) 902–907.

[24] M. Wang, H. Sun, M. Wang, L. Li, Understanding the "double-edged-sword" effect of dimethyl sulfoxide to guide the design of highly efficient perovskite solar cells in humid air, Nano Today 42 (2022) 101371, https://doi.org/10.1016/j.nantod.2021.101371.

[25] J. Li, J. Dagar, O. Shargaieva, M.A. Flatken, H. Köbler, M. Fenske, C. Schultz, B. Stegemann, J. Just, D.M. Többens, A. Abate, R. Munir, E. Unger, 20.8% slot-die coated MAPbI3 perovskite solar cells by optimal DMSO-Content and age of 2-ME based precursor inks, Adv. Energy Mater. 11 (10) (2021) 2003460, https://doi.org/10.1002/aenm.202003460.

[26] N.K. Noel, S.N. Habisreutinger, B. Wenger, M.T. Klug, M.T. Hörantner, M. B. Johnston, R.J. Nicholas, D.T. Moore, H.J. Snaith, A low viscosity, low boiling point, clean solvent system for the rapid crystallisation of highly specular perovskite films, Energy Environ. Sci. 10 (1) (2017) 145–152, https://doi.org/10.1039/c6ee02373h.

[27] I.H. Lee, Y.S. Shin, J. Han, J.-S. Nam, J.W. Song, D. Lee, J. Lee, J. Seo, J.G. Son, M. J. Sung, C.H. Yoon, M. Kim, J.A. Chae, W.K. Bae, J.Y. Kim, D.S. Kim, I. Jeon, A sweeter solution: caramelized sucrose additives render eco-friendly and high-performance perovskite solar cells, Adv. Energy Mater. 15 (32) (2025), https://doi.org/10.1002/aenm.202501911.

[28] Y. Bai, Q. Dong, Y. Shao, Y. Deng, Q. Wang, L. Shen, D. Wang, W. Wei, J. Huang, Enhancing stability and efficiency of perovskite solar cells with crosslinkable silane-functionalized and doped fullerene, Nat. Commun. 7 (2016) 12806, https://doi.org/10.1038/ncomms12806.

[29] S.V. Basenko, A.A. Maylyan, Unexpected reactions of dichloro(ethyl)silane with DMSO in organic solvents, Russ. Chem. Bull. 66 (5) (2017) 903–907.

[30] S.V. Basenko, I.A. Gebel, E.V. Boyarkina, M.G. Voronkov, Reaction of organylchlorosilanes with dimethyl sulfoxide in the presence of octamethyltrisiloxane, Russ. J. Gen. Chem. 74 (6) (2004) 9563958.

[31] S.V. Basenko, A.A. Maylyan, A.S. Soldatenko, New approach to the synthesis of symmetrical 1,3-Dichloro-1,1,3,3-Tetraorganyl- and 1,1,3,3-Tetrachloro-1,3-

diorganyldisiloxanes, Silicon 10 (2) (2016) 465–470, https://doi.org/10.1007/s12633-016-9474-0.

[32] S.K. Ignatov, P.G. Sennikov, A.G. Razuvaev, L.A. Chuprov, O. Schrems, B.S. Ault, Theoretical study of the reaction mechanism and role of water clusters in the gas-phase hydrolysis of SiCl4, J. Phys. Chem. A 107 (41) (2003) 8705–8713.

[33] H. Xiong, G. DeLuca, U. Bach, L. Jiang, Q. Zhang, E. Reichmanis, Y. Qiu, Synergistic effect of N,N-Dimethylformamide and hydrochloric acid on the growth of MAPbI(3) perovskite films for solar cells, ACS Omega 5 (50) (2020) 32295–32304, https://doi.org/10.1021/acsomega.0c04102.

[34] F. Wang, T. Wang, Y. Sun, X. Liang, G. Yang, Q. Li, Y. Li, X. Zhou, Q. Zhu, A. Ng, H. Lin, M. Yuan, Y. Shi, Tom Wu, H. Hu, Two-step perovskite solar cells with > 25% efficiency: unveiling the hidden bottom surface of perovskite layer, Adv. Mater. 36 (31) (2024) 2401476, https://doi.org/10.1002/adma.202401476.

[35] P. Scherrer, Bestimmung Der Grösse Und Der Inneren Struktur Von Kolloidteilchen Mittels Röntgenstrahlen, Nachrichten von der Gesellschaft der Wissenschaften, Göttingen, 1918, pp. 98–100.

[36] A. Guerrero, J. Bisquert, G. Garcia-Belmonte, Impedance spectroscopy of metal halide perovskite solar cells from the perspective of equivalent circuits, Chem. Rev. 121 (23) (2021) 14430–14484, https://doi.org/10.1021/acs.chemrev.1c00214.

[37] E.v. Hauff, D. Klotz, Impedance spectroscopy for perovskite solar cells: characterisation, analysis, and diagnosis, J. Mater. Chem. C 10 (2) (2022) 742–761, https://doi.org/10.1039/d1tc04727b.

[38] S. Ravishankar, Z. Liu, U. Rau, T. Kirchartz, Multilayer capacitances: how selective contacts affect capacitance measurements of perovskite solar cells, PRX Energy 1 (1) (2022) 013003, https://doi.org/10.1103/PRXEnergy.1.013003.